# Dislocation density distribution around an indent in single-crystalline nickel: Comparing nonlocal crystal plasticity finite-element predictions with experiments

C. Reuber [a], P. Eisenlohr [b], F. Roters [a,*], D. Raabe [a]

[a] *Max-Planck-Institut für Eisenforschung, Microstructure Physics and Alloy Design, Max-Planck-Straße 1, 40237 Düsseldorf, Germany*
[b] *Michigan State University, Chemical Engineering and Materials Science, East Lansing, MI 48824, USA*

## Abstract

We present a physics-based constitutive model of dislocation glide in metals that explicitly accounts for the redistribution of dislocations due to their motion. The model parameterizes the complex microstructure by dislocation densities of edge and screw character, which either occur with monopolar properties, i.e. a single dislocation with positive or negative line sense, or with dipolar properties, i.e. two dislocations of opposite line sense combined. The advantage of the model lies in the description of the dislocation density evolution, which comprises the usual rate equations for dislocation multiplication and annihilation, and formation and dissociation of dislocation dipoles. Additionally, the spatial redistribution of dislocations by slip is explicitly accounted for. This is achieved by introducing an advection term for the dislocation density that turns the evolution equations for the dislocation density from ordinary into partial differential equations. The associated spatial gradients of the dislocation slip render the model nonlocal. The model is applied to wedge indentation in single-crystalline nickel. The simulation results are compared to published experiments (Kysar et al., 2010) in terms of the spatial distribution of lattice rotations and geometrically necessary dislocations. In agreement with experiment, the predicted dislocation fluxes lead to accumulation of geometrically necessary dislocations around a vertical geometrical border with a high orientation gradient below the indenter that is decisive for the overall plastic response. A local model variant without dislocation transport is not able to predict the influence of this geometrical transition zone correctly and is shown to behave markedly softer.
© 2014 Acta Materialia Inc. Published by Elsevier Ltd. All rights reserved.

## 1. Introduction

The indentation of metals is widely used for material characterization and the derivation of mechanical properties [1–7]. Although the actual deformation process is simple, the boundary conditions and kinematics involved are complex. Accordingly, structure formation below indents is complex too, rendering the derivation of the corresponding structure–property relationship challenging. Hence, a thorough understanding of the underlying substructure evolution associated with indentation is of great importance.

One reason for the complexity of the deformation state is its strong variation both in space and time. Since the load of the indenter is locally applied, high gradients in the stress, strain and rotation fields naturally arise. As demonstrated by using 2-D and 3-D electron backscatter diffraction (EBSD) methods for a sphero-conical indenter, the loading of the material under the indenter changes with increasing indentation depth and induces a rapid change in the activated slip systems in space and time [8–14].

---

* Corresponding author. Tel.: +49 211 6792 393; fax: +49 211 6792 333.
 *E-mail address:* f.roters@mpie.de (F. Roters).

Variations in the plastic deformation also lead to a heterogeneous distribution of dislocations: regions of high plastic slip activity naturally contain more dislocations than weakly deformed regions. This relation between slip and the statistically stored dislocation (SSD) density can be described well by a local dislocation-based constitutive model [15–17]. If all dislocation loops are statistically equally distributed within and among the slip systems, then on average the signed character of the single dislocation segments mutually compensate and the ensemble of dislocations is neutral in the sense that no net Burgers vector (or plastic incompatibility) arises. A gradient in plastic slip, however, gives rise to an imbalance of dislocation segments of positive and negative sign, thus building up an excess of signed dislocations, also referred to as geometrically necessary dislocation (GND) density [18–25]. It is these GNDs that accommodate gradients in the lattice rotation field. However, they cannot confidently be predicted by a local constitutive law, since their origin—namely the redistribution of dislocations—is inherently nonlocal [26–30].

Initiated by the work of Walgraef and Aifantis [31], a new simulation approach has emerged in recent years; the so-called continuum density-based dislocation dynamics (CDDD) models treat dislocations as continuously defined dislocation density that evolves in time but also proceeds in space [32–35]. While similar in spirit, they differ in the degree of detail for the description of the dislocation density. A very detailed description is achieved when dislocations are represented by a higher-order dislocation density tensor that retains information about the line direction and the curvature [36]. With this description it is possible to formulate evolution laws for the dislocation density based only on the motion and balance equations of dislocations. When supplemented by a kinetic law, this formulation captures the kinematics of crystal plasticity in fine detail [37]. In order to reduce the substantial computational effort associated with such approaches, various simplifications were suggested to reduce this large configuration space: the restriction to two excess densities of edge and screw character plus their mean curvature and the total dislocation content [34], a single, but spatially variable line direction plus its mean curvature [35], the use of four density measures of straight edge and screw dislocations of opposite signs [31,33], or one excess density and the total dislocation density when restricting the model to two dimensions [38].

In our current approach, we develop a model that includes dislocation transport in a fashion similar to Arsenlis and Parks [33]. We apply this model to an existing microindentation experiment in single-crystalline Ni that was performed by Kysar et al. [39]. This experimental reference is chosen since the deformed volume in the experiment is, on the one hand, large enough so that statistical effects such as dislocation source sampling can be neglected; on the other hand, it is small enough so that dislocation transport is expected to play a significant role. We will analyze the effect of the dislocation transport in the simulations by means of a comparison with a local model variant without dislocation transport. The comparison to the experimentally obtained results then enables us to evaluate the generation of GNDs and their role in the mechanical response of the material.

The paper is organized as follows. In the next section we present the constitutive model with a description of the dislocation evolution equations, the dislocation kinetics and the integration into a finite strain framework. In Section 3 we introduce the setup of the experiment [39] and describe the implementation in the simulation. Section 4 presents the results both of the experiment and the simulations. A comparison of these results and a discussion follows in Section 5 with conclusions given in Section 6.

## 2. Constitutive model

### 2.1. Continuum mechanical framework of deformation

The description of the kinematics follows the established continuum mechanical framework of finite strain, as outlined, for instance, by Roters et al. [40]. The multiplicative decomposition of the deformation gradient

$$\boldsymbol{F} = \boldsymbol{F}_e \boldsymbol{F}_p \tag{1}$$

splits the deformation into a purely inelastic (or plastic) part, $\boldsymbol{F}_p$, and a remaining "elastic" part, $\boldsymbol{F}_e$, which accounts for elastic distortions of the crystal lattice and rigid body rotations [41]. Based on the right Cauchy–Green deformation tensor, an elastic strain measure is given by the Green–Lagrange strain tensor $\boldsymbol{E}_e$:

$$\boldsymbol{E}_e = \frac{1}{2}\left(\boldsymbol{F}_e^{\mathrm{T}}\boldsymbol{F}_e - \boldsymbol{I}\right), \tag{2}$$

with $\boldsymbol{I}$ the identity tensor. The second Piola–Kirchhoff stress $\boldsymbol{S}$ is related to this elastic strain tensor as its work-conjugate stress measure through:

$$\boldsymbol{S} = \det \boldsymbol{F}_e \; \boldsymbol{F}_e^{-1}\boldsymbol{\sigma}\boldsymbol{F}_e^{-\mathrm{T}} = \mathbb{C} : \boldsymbol{E}_e \tag{3}$$

with $\mathbb{C}$ being the fourth-order elasticity tensor and $\boldsymbol{\sigma}$ the Cauchy stress.

Plastic deformation is driven by $\boldsymbol{S}$ and in the present case is assumed to be mediated exclusively by dislocation glide on slip systems defined by two unit vectors $\boldsymbol{n}$ and $\boldsymbol{s}$ as the slip plane normal and slip direction with the latter being parallel to the respective Burgers vector $\boldsymbol{b}$ of length $b$. The shear rates $\dot{\gamma}^\xi$ resulting from corresponding changes in slipped area on systems $\xi = 1, \ldots, N$ contribute additively to the plastic velocity gradient $\boldsymbol{L}_p$ [42]:

$$\boldsymbol{L}_p = \sum_\xi \dot{\gamma}^\xi \; \boldsymbol{s}^\xi \otimes \boldsymbol{n}^\xi, \tag{4}$$

which in turn results in an evolution of the plastic deformation gradient at the rate:

$$\dot{\boldsymbol{F}}_p = \boldsymbol{L}_p \boldsymbol{F}_p. \tag{5}$$

The driving force for dislocation motion is provided by the resolved shear stress $\tau^\xi$:

$$\tau^\xi = \boldsymbol{S} : (\boldsymbol{s}^\xi \otimes \boldsymbol{n}^\xi), \tag{6}$$

which is the second Piola–Kirchhoff stress $\boldsymbol{S}$ projected onto the slip system.

## 2.2. The microstructure and its evolution: crystal orientation

The model is based on two main microstructural properties that describe the state of the material, namely orientations and dislocations. The first microstructural property is the crystal lattice and its orientation.

During deformation the orientation of the crystal lattice changes. The rotation that translates the initial crystal orientation $\boldsymbol{O}_0$ into the current crystal orientation $\boldsymbol{O}$ is referred to as crystal rotation $\boldsymbol{R}$.

$$\boldsymbol{O} = \boldsymbol{R}\boldsymbol{O}_0 \tag{7}$$

The current crystal orientation $\boldsymbol{O}$ rotates the laboratory coordinate system into the lattice coordinate system. It can be obtained by splitting the elastic deformation gradient $\boldsymbol{F}_e$ into a rotation part and a stretch $\boldsymbol{U}$ by means of a polar decomposition.

$$\boldsymbol{F}_e = \boldsymbol{O}^{\mathrm{T}}\boldsymbol{U} = (\boldsymbol{R}\boldsymbol{O}_0)^{\mathrm{T}}\boldsymbol{U} \tag{8}$$

Hence, the rotation tensor $\boldsymbol{R}$ is obtained by:

$$\boldsymbol{R} = \boldsymbol{U}^{-\mathrm{T}}\boldsymbol{F}_e^{\mathrm{T}}\boldsymbol{O}_0^{\mathrm{T}}. \tag{9}$$

## 2.3. The microstructure and its evolution: dislocation structure

The second microstructure parameter in the current model is the dislocation structure. Here, it is approximated by a set of densities $\varrho^\xi$ pertaining to the slip systems $\xi = 1, \ldots, N$. A distinction between the different densities on a specific slip system is made via the:

- dislocation character $c$: edge (subscript "e") or screw (subscript "s")
- dislocation polarity: monopolar density of positive or negative sign (subscript $+$ or $-$), or unsigned dipolar density (subscript $\pm$).

*Monopolar dislocation density.* A positive or negative sign reflects the monopolar nature of a single dislocation's stress field. Fig. 1 illustrates the convention adopted in this work for the sign of edge and screw dislocations on a slip plane. The signed character of these dislocations entails a directionality of their motion under a given resolved shear stress. According to Fig. 1, for a positive shear increment, i.e. increase in the slipped area by loop expansion, these directions of motion $\boldsymbol{m}$ follow as:

$$\boldsymbol{m}_{e+}^\xi = \boldsymbol{s}^\xi \tag{10a}$$

$$\boldsymbol{m}_{e-}^\xi = -\boldsymbol{s}^\xi \tag{10b}$$

$$\boldsymbol{m}_{s+}^\xi = \boldsymbol{n}^\xi \times \boldsymbol{s}^\xi \tag{10c}$$

$$\boldsymbol{m}_{s-}^\xi = -\boldsymbol{n}^\xi \times \boldsymbol{s}^\xi. \tag{10d}$$
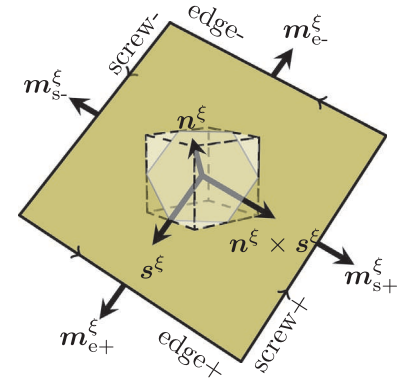


Fig. 1. Schematic dislocation loop (dark shade) on its slip plane with normal $\boldsymbol{n}^\xi$ and slip direction $\boldsymbol{s}^\xi$. Arrows along the loop periphery indicate positive line direction giving rise to the convention for signed dislocation characters as shown. The small (dashed) interior cube illustrates the crystal unit cell orientation. A displacement step by $\boldsymbol{b}^\xi$ occurs when passing from below to above the shaded slip plane, i.e. along its normal $\boldsymbol{n}^\xi$.

Accordingly, the plastic shear rate can be split into four parts for the four types $p \in \{e+, e-, s+, s-\}$ of monopolar dislocation populations.

$$\dot{\gamma}^\xi = \sum_p \dot{\gamma}_p^\xi = \sum_p \varrho_p^\xi v_p^\xi b \tag{11}$$

*Dipole dislocation density.* The presence of stable dipoles enables dislocation annihilation and is hence explicitly accounted for in the present parameterization. Stable dipoles contain two monopolar dislocations of the same character but opposite sign. Hence two dipole densities, $\varrho_{e\pm}^\xi$ and $\varrho_{s\pm}^\xi$, per slip system are tracked and sum up to the overall dipole density on slip system $\xi$:

$$\varrho_\pm^\xi = \varrho_{e\pm}^\xi + \varrho_{s\pm}^\xi. \tag{12}$$

These densities quantify the length per volume contributed by both constituents, thus dislocations changing between monopolar and dipolar state do not alter the total of both densities.

A dipole will be stable against dissociation under the resolved shear stress $\tau$ if the mutual elastic interaction between the two constituents is strong enough, i.e. if the distance between the glide planes of the two dislocations does not exceed:

$$\hat{d}_e = \frac{\mu\, b}{8\pi(1-v)} \frac{1}{|\tau|} \tag{13a}$$

$$\hat{d}_s = \frac{\mu\, b}{4\pi} \frac{1}{|\tau|} \tag{13b}$$

with $\mu$ the shear modulus and $v$ Poisson's ratio.

*Total and excess dislocation densities.* The polar nature of dislocation densities allows to discriminate between the accumulated (total) measures according to:

$$\varrho^\xi = \qquad \varrho_e^\xi \qquad + \qquad \varrho_s^\xi \tag{14a}$$

$$\varrho_e^\xi = \overbrace{\varrho_{e+}^\xi + \varrho_{e-}^\xi + \varrho_{e\pm}^\xi} \tag{14b}$$

$$\varrho_s^\xi = \qquad \overbrace{\varrho_{s+}^\xi + \varrho_{s-}^\xi + \varrho_{s\pm}^\xi} \tag{14c}$$

and the (either positive or negative) excess densities of edge and screw character

$$\varrho_{\Delta e}^{\xi} = \varrho_{e+}^{\xi} - \varrho_{e-}^{\xi} \tag{14d}$$

$$\varrho_{\Delta s}^{\xi} = \varrho_{s+}^{\xi} - \varrho_{s-}^{\xi}. \tag{14e}$$

*Forest dislocation density.* Following Ma and Roters [43], the density on any particular system $\zeta$ can be projected with respect to system $\xi$ into a corresponding forest density. By summation of the contribution of each slip system $\zeta$, the overall forest density on system $\xi$ results as:

$$\varrho_{f}^{\xi} = \varrho_{e}^{\zeta} \left| \boldsymbol{n}^{\xi} \cdot \left( \boldsymbol{n}^{\zeta} \times \boldsymbol{s}^{\zeta} \right) \right| + \varrho_{s}^{\zeta} \left| \boldsymbol{n}^{\xi} \cdot \boldsymbol{s}^{\zeta} \right| \tag{15}$$

The mean spacing between forest dislocations piercing through slip system $\xi$ can be derived from the forest dislocation density:

$$\lambda_{f}^{\xi} = \left( \varrho_{f}^{\xi} \right)^{-0.5} \tag{16}$$

### 2.3.1. Dislocation transport within a single crystal

The state of dislocation in a crystal lattice can be constructed from superposition of the contributions of all dislocation segments present in a given volume (including the case of multiple slip) as $\int \boldsymbol{l} \otimes \boldsymbol{b} \, d\varrho$, where $\boldsymbol{l}$ denotes a unit vector along the dislocation line direction. This state of dislocation corresponds to the Kröner–Nye tensor $\boldsymbol{\alpha}$ [19,18], which in turn is equivalent to the negative curl (incompatibility) of the plastic distortion $\boldsymbol{\beta}_p$. The contribution per individual slip system to this state reads:

$$\sum_{p} \varrho_{p}^{\xi} \boldsymbol{l}_{p}^{\xi} \otimes \boldsymbol{b} = \boldsymbol{\alpha}^{\xi} = -\mathrm{curl}\boldsymbol{\beta}_{p}^{\xi}. \tag{17}$$

Since segments of opposite line direction cancel out in above sum, only the excess density contributes to incompatibility.

$$\sum_{c} \varrho_{\Delta c} \boldsymbol{l}_{c+} \otimes \boldsymbol{b} = \boldsymbol{\alpha} = -\mathrm{curl}(\gamma \, \boldsymbol{n} \otimes \boldsymbol{s}), \tag{18}$$

where superscripts $\xi$ for the slip system were dropped (likewise in what follows). To arrive at the rate of change of the dislocation content, Eq. (18) is differentiated with respect to time $t$.

$$\partial_t (\varrho_{\Delta e} \boldsymbol{l}_{e+} + \varrho_{\Delta s} \boldsymbol{l}_{s+}) \otimes \boldsymbol{b} = -\mathrm{curl}(\dot{\gamma}/b \, \boldsymbol{n}) \otimes \boldsymbol{b} \tag{19}$$

Without loss of generality, we choose our coordinate system as shown in Fig. 1 to transform Eq. (19) into:

$$\partial_t \begin{pmatrix} \varrho_{\Delta s} \\ -\varrho_{\Delta e} \\ 0 \end{pmatrix} = -\mathrm{curl} \begin{pmatrix} 0 \\ 0 \\ \dot{\gamma}/b \end{pmatrix} = \begin{pmatrix} -\mathrm{grad}_t \dot{\gamma}/b \\ \mathrm{grad}_s \dot{\gamma}/b \\ 0 \end{pmatrix}, \tag{20}$$

which reflects the increase of (positive) excess density resulting from a (negative) gradient in the slip rate along the (positive) direction of dislocation motion:

$$\partial_t \varrho_{\Delta s} = -\mathrm{grad}_t (\varrho_{e+} \boldsymbol{v}_{e+} + \varrho_{e-} \boldsymbol{v}_{e-} + \varrho_{s+} \boldsymbol{v}_{s+} + \varrho_{s-} \boldsymbol{v}_{s-}) \tag{21a}$$

$$\partial_t \varrho_{\Delta e} = -\mathrm{grad}_s (\varrho_{e+} \boldsymbol{v}_{e+} + \varrho_{e-} \boldsymbol{v}_{e-} + \varrho_{s+} \boldsymbol{v}_{s+} + \varrho_{s-} \boldsymbol{v}_{s-}), \tag{21b}$$

where Eq. (11) was substituted for the shear rate.

To uncouple the equation system of all four dislocation types we note that the dislocation densities of same character but opposite sign evolve independently of each other:

$$\partial_t \varrho_{e+} + \mathrm{grad}_s (\varrho_{e+} \boldsymbol{v}_e) = -\kappa_{es} \, \mathrm{grad}_s (\varrho_s \boldsymbol{v}_s) \tag{22a}$$

$$\partial_t \varrho_{e-} - \mathrm{grad}_s (\varrho_{e-} \boldsymbol{v}_e) = (1 - \kappa_{es}) \, \mathrm{grad}_s (\varrho_s \boldsymbol{v}_s) \tag{22b}$$

and

$$\partial_t \varrho_{s+} + \mathrm{grad}_t (\varrho_{s+} \boldsymbol{v}_s) = -\kappa_{se} \, \mathrm{grad}_t (\varrho_e \boldsymbol{v}_e) \tag{22c}$$

$$\partial_t \varrho_{s-} - \mathrm{grad}_t (\varrho_{s-} \boldsymbol{v}_s) = (1 - \kappa_{se}) \, \mathrm{grad}_t (\varrho_e \boldsymbol{v}_e), \tag{22d}$$

with $\kappa_{es}$ and $\kappa_{se}$ denoting arbitrary fractions of 1. The right-hand side terms in Eqs. (22a)–(22d) reflect the fact that a gradient in slip caused by one character of dislocations results in changes in the other character (here, formation or annihilation of kinks). In the present treatment, such effects are considered to be of second order, which is tantamount to the assumption of straight dislocations that are not interconnected. Dropping these terms transforms the above evolution equations for the dislocation densities into pure transport equations.

$$\partial_t \varrho_{e+} + \mathrm{grad}_s (\varrho_{e+} \boldsymbol{v}_e) = 0 \tag{23a}$$

$$\partial_t \varrho_{e-} - \mathrm{grad}_s (\varrho_{e-} \boldsymbol{v}_e) = 0 \tag{23b}$$

and

$$\partial_t \varrho_{s+} + \mathrm{grad}_t (\varrho_{s+} \boldsymbol{v}_s) = 0 \tag{23c}$$

$$\partial_t \varrho_{s-} - \mathrm{grad}_t (\varrho_{s-} \boldsymbol{v}_s) = 0 \tag{23d}$$

In the following we denote the product of the dislocation density and velocity of type $p$ on slip system $\xi$ as dislocation flux $\boldsymbol{f}_p^{\xi} = \varrho_p^{\xi} \boldsymbol{v}_p^{\xi}$ with its scalar magnitude $f_p^{\xi} = \varrho_p^{\xi} \left| v_p^{\xi} \right|$. We can then summarize Eqs. (23a)–(23d) as:

$$\partial_t \varrho_p^{\xi} + \mathrm{div} \, \boldsymbol{f}_p^{\xi} = 0. \tag{24}$$

### 2.3.2. Dislocation generation

We regard multiple cross-slip of screw dislocations as the most relevant mechanism for dislocation generation. When identifying the obstacles that promote cross-slip with the dislocation forest, the multiplication rate due to multiple cross-slip of screws linearly depends on the inverse of the forest dislocation spacing. With $|\dot{\gamma}_s|/b$ as the rate of slipped area per volume due to glide of screw dislocations, one obtains the relationship:

$$_{\mathrm{mult}}\Phi_p \propto \frac{|\dot{\gamma}_s|}{b\lambda_f}. \tag{25}$$

In the following, any source or sink term for the dislocation density will be denoted by $\Phi$ and goes to the right-hand side of Eq. (24).

Dislocations of edge type contribute to a minor extent to the production of new dislocation line length by loop expansion. Hence, we define an effective multiplication rate $_{\mathrm{mult}}\Phi_p$ for the total dislocation generation

$$_{\mathrm{mult}}\Phi_p = \frac{|k_1\dot{\gamma}_e + \dot{\gamma}_s|}{k_2 b \lambda_f} = \frac{(k_1 f_e + f_s)\sqrt{\varrho_f}}{k_2}, \tag{26}$$

with $0 < k_1 \leq 1$ as a parameter that controls the edge contribution to dislocation generation, and with a second (phenomenological) scaling parameter $10 \lesssim k_2 \lesssim 100$.

### 2.3.3. Formation and dissociation of dislocation dipoles

*Dipole formation.* A dipole is formed if a gliding dislocation encounters a dislocation of opposite sign within a distance closer than $\hat{d}$. Monopolar density can transform by either actively moving towards an opposite dislocation, or by passively having an opposite dislocation move towards itself. These two configurations lead to a combined transformation loss rate of monopolar dislocations of:

$$_{\text{mo}\rightarrow\text{di}}\Phi_{c+} = -2\hat{d}_c(\varrho_{c-}f_{c+} + \varrho_{c+}f_{c-}) \tag{27a}$$

$$_{\text{mo}\rightarrow\text{di}}\Phi_{c-} = -2\hat{d}_c(\varrho_{c+}f_{c-} + \varrho_{c-}f_{c+}). \tag{27b}$$

Since the total dislocation content is not changed by such transformations, the corresponding rate of change (production) of dipolar density follows as the negative sum of Eqs. (27a) and (27b).

$$_{\text{mo}\rightarrow\text{di}}\Phi_{c\pm} = 4\hat{d}_c(\varrho_{c+}f_{c-} + \varrho_{c-}f_{c+}) \tag{27c}$$

*Dipole dissociation.* Dipoles that were formed by gliding monopolar dislocations can dissociate again when the stress level increases. If we assume that the distribution of dipole heights is uniform within the stability range, then a reduction in the upper stability limit due to increasing resolved shear stress will lead to a symmetric dissociation of dipoles back into monopolar dislocation density.

$$_{\text{di}\rightarrow\text{mo}}\Phi_{c\pm} = \varrho_{c\pm}\frac{\min\{\partial_t\hat{d}_c; 0\}}{\hat{d}_c - \check{d}_c} \tag{28a}$$

$$_{\text{di}\rightarrow\text{mo}}\Phi_{c+} = {_{\text{di}\rightarrow\text{mo}}\Phi_{c-}} = -\frac{1}{2}{_{\text{di}\rightarrow\text{mo}}\Phi_{c\pm}} \tag{28b}$$

### 2.3.4. Dislocation annihilation

Due to the low self-diffusivity of Ni at room temperature, we neglect thermally activated annihilation by climb of edge dislocations. Hence, a decrease in the overall dislocation density is considered a result of athermal annihilation of close dipoles that have a glide plane separation below $\check{d}_e$ [44]. The corresponding rate reads:

$$_{\text{athAnn}}\Phi_{e\pm} = -4\check{d}_e(\varrho_{e+}f_{e-} + \varrho_{e-}f_{e+}) - 2\check{d}_e\varrho_{e\pm}(f_{e-} + f_{e+}), \tag{29}$$

where the second term accounts for close encounters of monopolar dislocations with one constituent of a dipole.

Screw dipoles can annihilate by cross-slip [45]. While this process can be thermally activated, we assume it to take place instantaneously for all screw dipoles having a glide plane separation below $\check{d}_s$, given the high stacking-fault energy of Ni. Consequently, the cross-slip process of screw dipoles is treated in the same manner as the athermal disintegration of edge dipoles.

$$_{\text{cross}}\Phi_{s\pm} = -4\check{d}_s(\varrho_{s+}f_{s-} + \varrho_{s-}f_{s+}) - 2\check{d}_s\varrho_{s\pm}(f_{s-} + f_{s+}) \tag{30}$$

However, the minimum glide plane separation that controls these two mechanisms can differ significantly (see Table 1).

While the annihilation of edge dipoles produces vacancies or interstitials, screw dipoles that annihilate by cross-slip deposit two edge jogs on the collinear slip system. Each annihilated screw dipole creates two edge jogs of length equal to the mean dipole height

$$l_{\text{jog}} = \frac{1}{2}(\hat{d}_s + \check{d}_s). \tag{31}$$

The number of screw dipoles that annihilate by cross-slip can be determined from the cross-slip annihilation rate $_{\text{cross}}\Phi_{s\pm}$, if one assumes that the average segment length of a screw dipole is proportional to the forest spacing. Then, screw dipoles of the primary slip system $\xi$ that annihilate by cross-slip generate an average density of both positive and negative edges on the according collinear slip system $\zeta$:

Table 1
Constitutive parameters of single-crystalline nickel used for the simulation of the wedge indent.

| Property | | Value | Unit | Ref. |
|---|---|---|---|---|
| Cubic elasticity constants | $C_{11}$ | 246.5 | GPa | Hirth and Lothe [51] |
| | $C_{12}$ | 147.3 | GPa | Hirth and Lothe [51] |
| | $C_{44}$ | 124.7 | GPa | Hirth and Lothe [51] |
| Isotropic shear modulus | $\mu$ | 94.66 | GPa | Hirth and Lothe [51] |
| Poisson ratio | $v$ | 0.277 | | Hirth and Lothe [51] |
| Length of Burgers vector | $b$ | 0.248 | nm | Cordero et al. [55] |
| Min. dipole separation edge | $\check{d}_e$ | 2.6 | nm | Tippelt et al. [52] |
| Min. dipole separation screw | $\check{d}_s$ | 12 | nm | |
| Mean free path prefactor | $k_2$ | 45 | | |
| Edge multiplication factor | $k_1$ | 0.1 | | |
| Initial dislocation density | $\varrho_0$ | $2.88 \cdot 10^{12}$ | $m^{-2}$ | |
| Solid-solution activation energy | $Q_S$ | 1.12 | eV | |
| Solid-solution concentration | $c_{at}$ | $5 \cdot 10^{-7}$ | | |
| Solid-solution strength | $\tau_S$ | 8.3 | MPa | |
| Attack frequency | $v_a$ | 50 | GHz | |
| Dislocation mobility | $B$ | 0.248 | $ms^{-1} MPa^{-1}$ | |
| Edge jog formation factor | $k_3$ | 0.01 | | |

$$_{\text{jog}}\Phi^{\zeta}_{\text{e}+} = {}_{\text{jog}}\Phi^{\zeta}_{\text{e}-} = -k_3 \frac{_{\text{cross}}\Phi^{\xi}_{\text{s}\pm}}{2} \frac{l_{\text{jog}}}{\lambda_{\text{f}}}$$

$$= -\frac{k_3}{4}\sqrt{\varrho^{\xi}_{\text{f}}}\left(\hat{d}^{\xi}_{\text{s}} + \check{d}^{\xi}_{\text{s}}\right)_{\text{cross}}\Phi^{\xi}_{\text{s}\pm}, \qquad (32)$$

where $k_3$ is a scalar factor between 0 and 1.

### 2.3.5. Summary of dislocation density evolution equations

The equations derived above form a system of partial differential equations (PDEs) with the local rate equations for generation, annihilation, and state change as sink or source terms. Hence, for each slip system $\xi$ we have the following set of PDEs:

$$\partial_t \varrho^{\xi}_{\text{e}+} + \text{div} \boldsymbol{f}^{\xi}_{\text{e}+} = {}_{\text{mult}}\Phi^{\xi}_{\text{e}+} + {}_{\text{mo}\to\text{di}}\Phi^{\xi}_{\text{e}+} + {}_{\text{di}\to\text{mo}}\Phi^{\xi}_{\text{e}+} + {}_{\text{jog}}\Phi^{\xi}_{\text{e}+} \quad (33\text{a})$$

$$\partial_t \varrho^{\xi}_{\text{e}-} + \text{div} \boldsymbol{f}^{\xi}_{\text{e}-} = {}_{\text{mult}}\Phi^{\xi}_{\text{e}-} + {}_{\text{mo}\to\text{di}}\Phi^{\xi}_{\text{e}-} + {}_{\text{di}\to\text{mo}}\Phi^{\xi}_{\text{e}-} + {}_{\text{jog}}\Phi^{\xi}_{\text{e}-} \quad (33\text{b})$$

$$\partial_t \varrho^{\xi}_{\text{s}+} + \text{div} \boldsymbol{f}^{\xi}_{\text{s}+} = {}_{\text{mult}}\Phi^{\xi}_{\text{s}+} + {}_{\text{mo}\to\text{di}}\Phi^{\xi}_{\text{s}+} + {}_{\text{di}\to\text{mo}}\Phi^{\xi}_{\text{s}+} \quad (33\text{c})$$

$$\partial_t \varrho^{\xi}_{\text{s}-} + \text{div} \boldsymbol{f}^{\xi}_{\text{s}-} = {}_{\text{mult}}\Phi^{\xi}_{\text{s}-} + {}_{\text{mo}\to\text{di}}\Phi^{\xi}_{\text{s}-} + {}_{\text{di}\to\text{mo}}\Phi^{\xi}_{\text{s}-} \quad (33\text{d})$$

$$\partial_t \varrho^{\xi}_{\text{e}\pm} = {}_{\text{athAnn}}\Phi^{\xi}_{\text{e}\pm} + {}_{\text{mo}\to\text{di}}\Phi^{\xi}_{\text{e}\pm} + {}_{\text{di}\to\text{mo}}\Phi^{\xi}_{\text{e}\pm} \quad (33\text{e})$$

$$\partial_t \varrho^{\xi}_{\text{s}\pm} = {}_{\text{cross}}\Phi^{\xi}_{\text{s}\pm} + {}_{\text{mo}\to\text{di}}\Phi^{\xi}_{\text{s}\pm} + {}_{\text{di}\to\text{mo}}\Phi^{\xi}_{\text{s}\pm} \quad (33\text{f})$$

### 2.4. Dislocation kinetics

The driving force for the in-plane motion of dislocations is the resolved shear stress $\tau$ as defined in Eq. (6). The glide motion of dislocations is impeded by various obstacles, of which some may be overcome by thermal activation, and some by mechanical stresses alone.

The mutual interaction of dislocations is considered too strong as to allow for thermal activation. Hence, we describe the effect of dislocation obstacles in terms of a mechanical threshold stress, referred to as the critical resolved shear stress $\tau_{\text{cr}}$. For an applied resolved stress below this value no dislocation activity occurs. Above this threshold, an effective resolved shear stress $\tau_{\text{eff}}$ that is reduced by the critical resolved shear stress is acting as driving force for dislocation motion [46].

$$\tau_{\text{eff}} = \begin{cases} (|\tau| - \tau_{\text{cr}})\,\text{sign}\,\tau & \text{if } |\tau| > \tau_{\text{cr}} \\ 0 & \text{if } |\tau| \leqslant \tau_{\text{cr}} \end{cases} \qquad (34)$$

The flow stress $\tau_{\text{cr}}$ accounts for the different strength $a^{\xi\zeta}$ of the reaction products of the interacting dislocations on slip systems $\xi$ and $\zeta$ [47].

$$\tau^{\xi}_{\text{cr}} = \mu b \sqrt{\sum_{\zeta} a^{\xi\zeta} \varrho^{\zeta}} \qquad (35)$$

In the case of face-centered cubic (fcc) crystals, six distinct reactions with characteristic strength can be identified. Values for junction and lock forming are taken from Kubin et al. [48]. However, in contrast to Kubin et al. [48], we assume the coefficients for the self-interaction and the coplanar interaction to be equal to zero. Instead, self-hardening is implied by the sink term for the monopolar density due to formation of dipoles, which decreases the amount of the

available carrier density for dislocation slip (see Eqs. (27a) and (27b)). A second source for self-hardening stems from the deposition of edge jogs on the cross-slip plane due to the annihilation of screw dipoles as described in Section 2.3.4. These edge jogs act back on the primary slip system via the strong collinear interaction contributing to self-hardening.

In addition to dislocation obstacles, we consider solid solution atoms of concentration $c_{\text{at}}$ as further obstacles against dislocation motion. Thermal activation of this effect is treated according to Kocks et al. [49]. The probability $P$ of overcoming an obstacle by thermal activation at temperature $T$ is given by:

$$P = \exp\left(-\frac{Q_{\text{S}}}{k_{\text{B}}T}\left(1 - \frac{|\tau_{\text{eff}}|}{\tau_{\text{S}}}\right)\right), \qquad (36)$$

where $Q_{\text{S}}$ is the activation energy required to overcome the obstacle and $\tau_{\text{S}}$ is its strength. Then, the waiting time $t_{\text{w}}$ in front of an obstacle is determined by the product of the attempt frequency $v_{\text{a}}$ and the success probability $P$.

$$t_{\text{w}} = \frac{1}{v_{\text{a}}P} \qquad (37)$$

After a successful event the dislocation will on average travel a distance that is equal to the mean spacing between obstacles $\lambda_{\text{S}} = \frac{b}{\sqrt{c_{\text{at}}}}$. The travel time for this distance depends on the travel velocity $v_{\text{t}}$, which is considered as linear viscous drag law with mobility $B$.

$$v_{\text{t}} = B|\tau_{\text{eff}}| \qquad (38)$$

The effective velocity can then be determined from the waiting time at an obstacle and from the travel velocity between the obstacles.

$$v = \frac{\lambda_{\text{s}}}{t_{\text{w}} + \frac{\lambda_{\text{s}}}{v_{\text{t}}}}$$

$$= \left[\frac{\sqrt{c_{\text{at}}}}{bv_{\text{a}}}\exp\left(\frac{Q_{\text{S}}}{k_{\text{B}}T}\left(1 - \frac{|\tau_{\text{eff}}|}{\tau_{\text{S}}}\right)\right) + \frac{1}{B|\tau_{\text{eff}}|}\right]^{-1}\text{sign}\,\tau \qquad (39)$$

## 3. Problem setup

As a suitable reference example for comparing simulations with experiment we use an elegant wedge indentation study published by Kysar et al. [39] (a more detailed view on the same experiment has recently been published by Dahlberg et al. [50]). In this experimental work, pure single-crystalline fcc Ni was indented by a 90° wedge indenter to an indentation depth of about 200 μm. The indent was placed into a (001)-oriented surface; the indenter axis was aligned parallel to the [110] lattice direction (see Fig. 2). Kysar et al. [39] suggest that these specific loading conditions lead to a plane-strain deformation state. After indentation, the sample was cut in half normal to the wedge indent and the exposed surface was analyzed by EBSD.
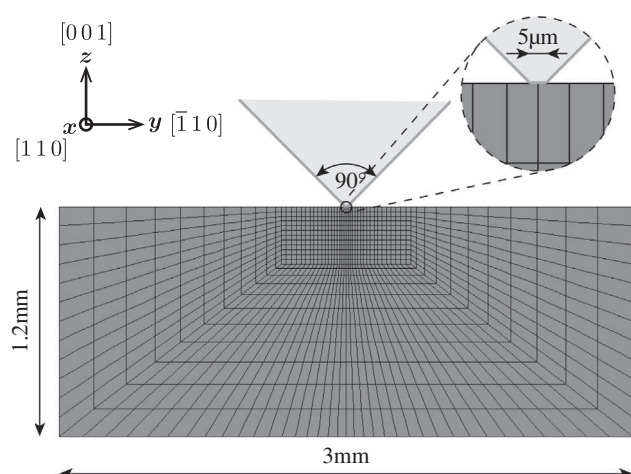
Fig. 2. FE mesh used for the simulation of wedge indentation. The indenter is modeled by two flat surfaces that have an inclination angle of 90° and a flat tip of 5 μm width.
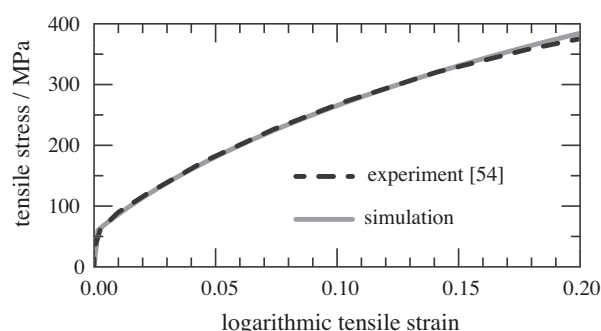


Fig. 3. Stress–strain curve of a tensile test of a polycrystalline sample. Experimental data was reproduced from Keller et al. [54] and used for fitting of the material parameters.

The experiment is modeled by a FE simulation with a planar mesh of 1092 hexahedral elements with quadratic interpolation functions and reduced integration capacity (Fig. 2). Except for the indented surface, all nodes on the outer surfaces of the model were constrained to in-plane motion, i.e. no displacement normal to the respective surface was allowed. In particular, displacement in the direction of the wedge indent was constrained to be zero on the front and back surface in Fig. 2 in order to mimic plane-strain conditions. Due to the plane-strain conditions the mesh is only one element thick. The lateral extent of the FE mesh does not cover the complete sample domain (which was approximately $1 \times 1 \times 1$ cm$^3$), but is chosen sufficiently large for the boundaries to not influence the predictions. The wedge indenter was modeled by two rigid surfaces that form an angle of 90° and a flat tip surface of 5 μm width (see blow-up in Fig. 2). The exact shape of the indenter tip does not, however, play an important role as long as the tip geometry is smaller than the minimum distance between nodes, since in the simulation a contact condition is evaluated only at and not in between nodes.[1] Contact conditions between the indenter and material surface were modeled by Coulomb friction with a friction coefficient of 0.3.

The sample coordinate system is chosen such that the indentation proceeds in negative $z$ direction and the indenter axis is parallel to the $x$ direction. This implies an orientation of the single crystal of $\varphi_1 = 315°$, $\phi = 0°$, $\varphi_2 = 0°$ expressed in Bunge notation, such that in the reference configuration the [1 1 0] direction corresponds to the $x$ axis, the [$\bar{1}$ 1 0] direction to the $y$ axis and the [0 0 1] direction to the $z$ axis.

Elastic constants of Ni are taken from Hirth and Lothe [51]. An experimentally obtained value for the minimum dipole separation distance $\breve{d}_e$ is taken from Tippelt et al. [52]. The self-diffusivity of Ni at room temperature was calculated on the basis of material parameters from Gottstein [53]; however, the self-diffusivity at room temperature is small enough so that dislocation climb can be neglected. All other material parameters have to be fitted to experimental data, but have clear physical bounds. Apart from a force–displacement measurement of the actual indentation experiment, Kysar et al. [39] do not provide further material characteristics of the sample. Therefore, data from uniaxial tensile tests of highly pure polycrystalline Ni taken from Keller et al. [54] were used to fit the material parameters of the model. The stress–strain curves of both experiment and fitting simulation can be seen in Fig. 3. A list of all material parameters is given in Table 1.

## 4. Results obtained from comparing wedge indentation simulations with experiment

### 4.1. Load–displacement response

Fig. 4 compares the load–displacement response of the indentation experiment to two simulations, one with the nonlocal model and one with a local model variant that does not include the transport term. Surprisingly, the local simulation results perfectly match the experiment for small indentation depth up to a displacement of about 75 μm. However, for larger displacements above 75 μm, the experimental load–displacement curve becomes notably steeper as compared to the simulation, such that the maximum load for the local simulation is about 28% lower than in the experiment. In general, the nonlocal simulation reveals larger forces than the local simulation; hence, the maximum load is closer to the experiment. However, similar to the local simulation, the slope of the load–displacement curve deviates significantly from the experiment in not showing a distinct increase at larger indentation depths. One main reason for this might be the improper account of friction forces. Although the friction coefficient was

---

[1] While Kysar et al. [39] report a tip radius of 100 nm for the indenter that was used in experiment, Dahlberg et al. [50] used a tip radius of 100 μm for their simulation of the same experiment.
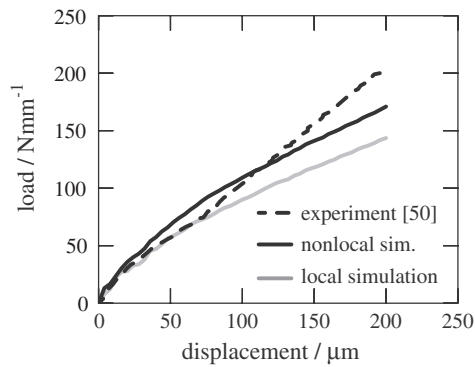
Fig. 4. Load–displacement curves of the wedge indent in single-crystalline nickel. Dotted curve represents experimental values reproduced from Dahlberg et al. [50], solid black and gray lines are nonlocal and local simulation results, respectively.

chosen comparably high at a value of 0.3, the influence on the forces was found to be marginal (at zero friction the maximum load reduces by merely 2%). This indicates that the influence of friction is underestimated in the simulation. Since the friction force is expected to grow proportionally with the displacement [56], this could explain the deviations at higher deformations. Another probable source of error is the fitting of the material parameters against tensile test data of not exactly the same material as used in the indentation experiment. Also, the tensile test specimens in Keller et al. [54] had a mean grain size of 40 μm, which could give rise to a visible grain size effect. Since the fitting simulations are based on the local model, such a grain size effect would not have been taken properly into account, which may be one explanation for the systematic overestimation of forces at small deformation in the nonlocal indentation simulations.

## 4.2. Lattice rotation and GND density

In addition to the load–displacement curve, Kysar et al. [39] measured the lattice rotations around the indent by

EBSD. Fig. 5 juxtaposes maps of the experimentally obtained lattice rotation in the $yz$ plane and the simulated rotation maps. Both reveal the same features, although, in general, the simulation slightly overestimates the rotations compared to the experiment. Regions of high rotation can be found on both flanks of the indent and directly below the tip of the indent. A boundary running vertically down from the indenter tip divides the sample into two halves with symmetric rotation patterns but inverted sign. The out-of-plane rotations were negligibly small both in experiment and simulation.

The observation that the absolute values of the rotations are higher in the simulations compared to the experiments can be explained in terms of the fact that the highest reorientation would be expected to occur close to the interface between indenter and crystal. However, the metallographic preparation required for the EBSD characterization leads to a modest curvature of the sample edges. Hence, the contact area between indenter and sample cannot be mapped.

From the experimentally obtained lattice rotations Kysar et al. [39] derived lower bounds for the $L_1$ norm of the GND density, i.e. for the sum of the absolute values of edge and screw GNDs over all slip systems. This lower bound is equivalent to the actual value when only one or two effective slip systems are active. The obtained map of GND density is shown on the left-hand side of Fig. 6 with the corresponding $L_1$ norm of the simulated excess dislocation density on the right. The experimental and simulated dislocation densities match very well both qualitatively and quantitatively. In particular, both reveal the highest densities of GNDs around the evolving border beneath the indenter. To both sides of this boundary, GNDs of about 10 times lower density extend into the material and form bands that draw an angle of about ±45° with the deformation-induced boundary. The same feature with similar angles occurs in the simulation, yet not as finely structured due to the limited mesh resolution and the disregard of the discreteness in dislocation sources. While
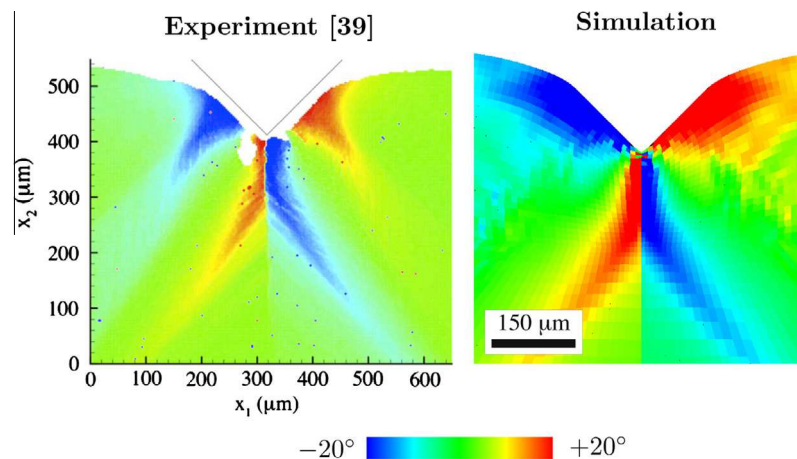


Fig. 5. In-plane lattice rotation as obtained from experiment [39] and from simulation.
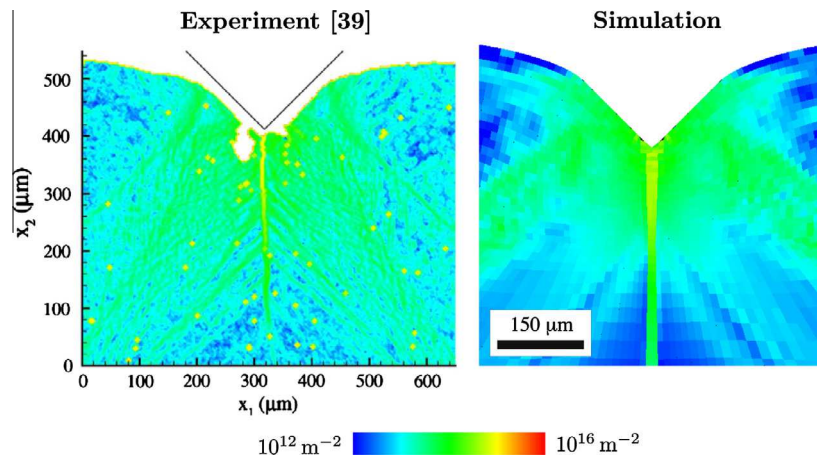
Fig. 6. GND density as obtained from experiment [39] and from simulation on a logarithmic scale.

in the experiment no detailed description of the GND distribution on the individual slip systems was possible, the simulation provides information about this distribution with respect to slip system and dislocation character (edge and screw) as shown in Fig. 7.

### 4.3. Strain and stress state

In order to understand the material behavior, especially with respect to dislocation activity, it is helpful to map the strain and stress state below the indenter.

Fig. 8 shows a map of the simulated von Mises logarithmic strain after unloading. It reveals several distinct regions of concentrated strain and a symmetric distribution with respect to the vertical indentation axis. The highest strains of about 1 occur directly under the indenter tip. Around the tip we observe a triangular region with still comparably high strains around 0.5 that encloses approximately the same area as the actual indent. Within this central region two deformation modes prevail. Directly under the indenter tip the material deforms by compression in the $z$ direction and extension in the $y$ direction (see right side of Fig. 8). In the lateral corners of the triangle the material rather deforms by simple shear. Two regions of slightly lower equivalent strain are visible on both sides of the symmetry axis. They have a beam-like shape that points away from the symmetry axis at an angle of nearly 45° and extends into the sample to approximately five times the indentation depth. The first region, which connects to the lower sides of the central triangular region, exhibits the same deformation mode as under the indenter tip, namely compression in the $z$ direction and extension in the $y$ direction. The second region, which starts slightly below the flank of the indent, reveals biaxial strain with extension in the $z$ direction and compression in $y$ direction. In between these strain concentrations, the material stays almost undeformed with $\varepsilon \lesssim 0.1$.

Fig. 9 shows the equivalent Cauchy stress just before unloading (left) and after unloading (right). In both the loaded and unloaded condition there are mainly two different regimes (however, this differentiation is less pronounced for the unloaded situation). In a circular area of about the indentation depth around the indenter the material faces almost pure hydrostatic pressure. Around this central area of hydrostatic pressure, the stress has uniaxial compressive character. The principal direction of this compressive stress points radially away from the central regime. This means that on the indentation axis the compressive stress acts in the $z$ direction, i.e. in the direction of the evolving boundary, while close to the material surface the principal axis of the stress lies almost parallel to the $y$ axis. The highest stress occurs in between these two positions when the principal stress axis makes a 45° angle with the indentation axis, i.e. is perpendicular to the indenter flanks.

While the highest strain is found in a circular area directly under the indenter, the highest stress values are found around this area. It is just at the edge of these two areas where most of the plastic shear occurs, as will be discussed next.

### 4.4. Plastic slip

The deformation of the material under the indenter is accomplished by only six slip systems (Table 2). All other systems do not significantly contribute to plastic deformation. As shown by Rice [57] and in detail for the current geometry by Kysar et al. [39], the six active slip systems form three pairs of "partner" slip systems that cooperatively accomplish a plane-strain deformation when subjected to a line load along the [110] direction. The two collinear slip systems 3 and 6 in combination allow for slip in the direction of [1$\bar{1}$0] on an effective slip plane (001), hence shear in the (110) plane. The two coplanar slip systems 7 and 8 in combination allow for slip in an effective direction [1$\bar{1}$2] on the slip plane (1$\bar{1}$$\bar{1}$), hence also shear in the (110) plane. Finally, the two coplanar slip systems 10 and 11 in combination allow for slip in an effective direction [$\bar{1}$12] on the slip plane ($\bar{1}$1$\bar{1}$), hence again shear in the
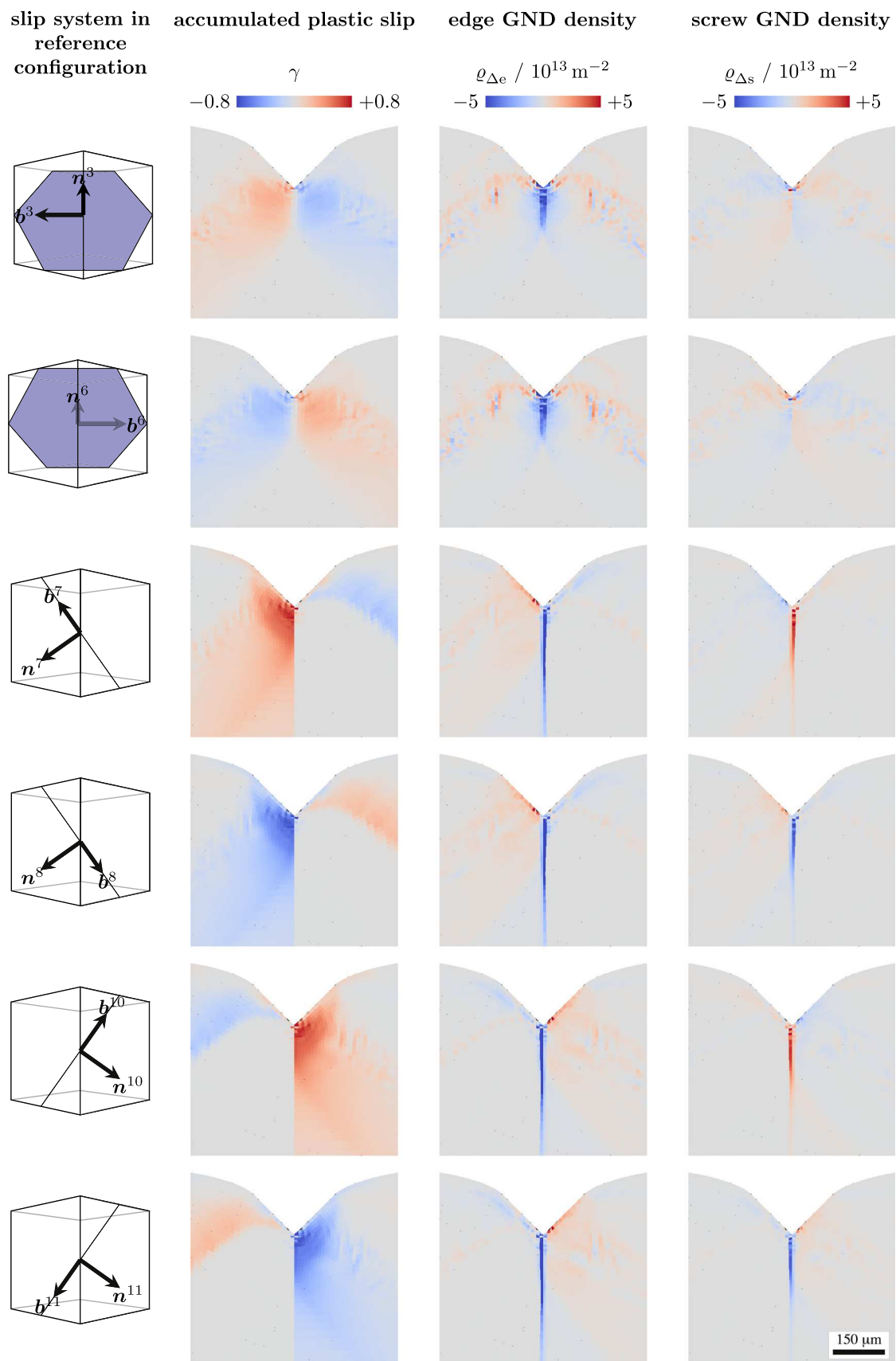
| slip system in reference configuration | accumulated plastic slip | edge GND density | screw GND density |
|---|---|---|---|

$$\gamma$$

$$-0.8 \quad \blacksquare \quad +0.8$$

$$\varrho_{\Delta e} \ / \ 10^{13} \, \mathrm{m}^{-2}$$

$$-5 \quad \blacksquare \quad +5$$

$$\varrho_{\Delta s} \ / \ 10^{13} \, \mathrm{m}^{-2}$$

$$-5 \quad \blacksquare \quad +5$$

Fig. 7. Simulated accumulated plastic shear and GND densities for the six active slip systems below the wedge indent.
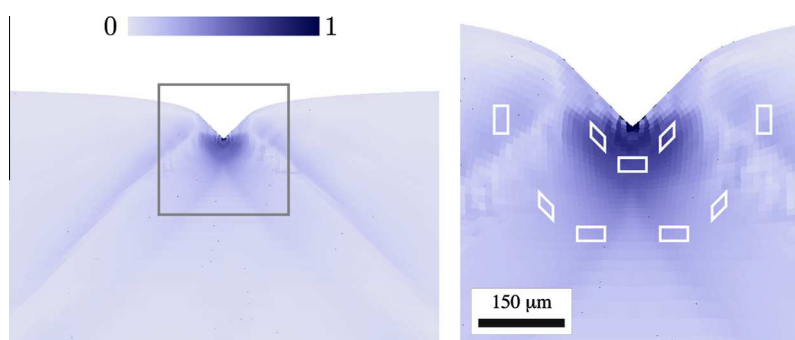
Fig. 8. Simulated von Mises logarithmic strain distribution with schematic representation of the predominant deformation modes around the wedge indent.

(1 1 0) plane. All six observed activated slip systems lead to a plane-strain deformation in the (1 1 0) lattice plane, which is normal to the lab $x$ axis. The exact distribution of the accumulated plastic slip on the six active slip systems is shown in the second column of Fig. 7. The two "partner" slip systems cover the same regions of activity, but with inverted signs of the accumulated slip due to the symmetric orientation of the two slip systems with respect to the indentation axis. The most striking feature of the maps for slip systems 7/8 and 10/11 is the sharp edge of the slipped volume right below the indenter tip, which is in contrast to the gradual decay in slip activity elsewhere.

Fig. 10 shows the evolution of the shear rate on three of the active slip systems with increasing indentation depth; the shear rate on the other slip systems follows from inversion of sign. On slip system 6, plastic slip starts in two bands that point away from the (undeformed sample) surface at a 45° angle. With increasing indentation these microbands of concentrated slip become broader, less intense, and move downwards. At the same time, a region of no slip activity expands around the indenter tip. This corresponds to the hydrostatic pressure regime seen in Fig. 9 that does not provide any resolved shear stress for plastic slip. The slip activity on slip system 8 also starts in two bands of 45° from the surface. However, the active regions evolve differently on both sides of the rotation boundary. The red band on the right is moving up while keeping its relative position on the indenter flank. The blue band on the left side splits up into two branches with an inflection point at the boundary that moves down. The upper branch describes an arc towards a point at the same relative position on the indenter flank as where the red band starts at on the left side. With increasing indentation, the arc bows out, leaving behind a region of virtually no slip activity similarly to what can be seen for slip system 6. The lower branch of the active region becomes broader to the bottom with increasing indentation and rotates towards the indentation axis. The slip activity on system 10 evolves accordingly, with reflection at the indentation axis and inversion of sign.

## 5. Discussion

### 5.1. Analogy to closing crack

Saito and Kysar [58] proposed an analogy between the stress and deformation fields around a closing crack and those around the moving contact singularity at the indenter flanks, where the indenter loses contact with the surface. They derive analytical expressions for the stress field around the singularity if the included angle of the indenter approaches 180°. It turns out that for an ideally plastic material this implies that plasticity occurs in confined rays that emanate from the contact singularity under certain angles, which can be determined analytically. In a companion paper, Saito et al. [59] could verify these characteristics
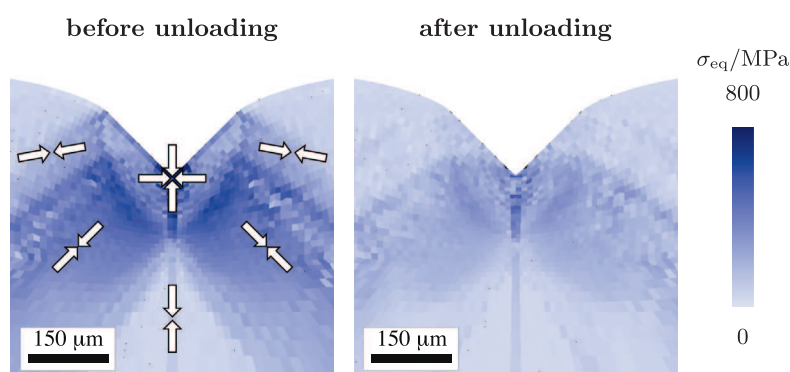


Fig. 9. Simulated von Mises Cauchy stress around the wedge indent before and after unloading. Main stress states are indicated by white arrows.

Table 2
Face-centered cubic slip systems used in the simulations. Active slip systems are listed in black, all others in light gray.

| $\xi$ | Slip plane | Slip direction | System number as in [39] |
|---|---|---|---|
| 1 | (1 1 1) | [0 1 $\bar{1}$] | |
| 2 | (1 1 1) | [$\bar{1}$ 0 1] | |
| 3 | (1 1 1) | [1 $\bar{1}$ 0] | 2 |
| 4 | ($\bar{1}$ $\bar{1}$ 1) | [0 $\bar{1}$ $\bar{1}$] | |
| 5 | ($\bar{1}$ $\bar{1}$ 1) | [1 0 1] | |
| 6 | ($\bar{1}$ $\bar{1}$ 1) | [$\bar{1}$ 1 0] | 2 |
| 7 | (1 $\bar{1}$ $\bar{1}$) | [0 $\bar{1}$ 1] | 3 |
| 8 | (1 $\bar{1}$ $\bar{1}$) | [$\bar{1}$ 0 $\bar{1}$] | 3 |
| 9 | (1 $\bar{1}$ $\bar{1}$) | [1 1 0] | |
| 10 | ($\bar{1}$ 1 $\bar{1}$) | [0 1 1] | 1 |
| 11 | ($\bar{1}$ 1 $\bar{1}$) | [1 0 $\bar{1}$] | 1 |
| 12 | ($\bar{1}$ 1 $\bar{1}$) | [$\bar{1}$ 1 0] | |

of the deformation field for simulations with a phenomenological crystal plasticity model. The plasticity model used in this work results in very similarly oriented plastic rays emanating from the contact singularity point, as can be seen from the match against the analytically predicted angles [58] that are shown as an overlay in Fig. 10.

## 5.2. Active slip systems

In order to understand the evolution of lattice rotations and GND densities it is useful to have a closer look at the evolution of plastic slip on the individual slip systems. As pointed out above, the stress that drives dislocation motion is of almost pure uniaxial compressive nature with the principal axis pointing radially away from a central region of

hydrostatic pressure and no slip activity. The highest stress values are found in two regions left and right of the inter axis, where the principal stress direction makes a 45° angle with the rotation boundary. A positive lattice rotation around the $x = [1\ 1\ 0]$ direction (or a negative rotation of the principal stress axis) increases the Schmid factor of systems 10 and 11 on the right side and decreases the Schmid factor of systems 7 and 8. The opposite holds for inverted rotation sense or on the other side of the indentation axis. Slip systems 3 and 6 initially have their highest possible Schmid factors with respect to a rotation around the [1 1 0] direction for a 45° principal stress axis, so that any change in the lattice orientation or the principal stress axis decreases the Schmid factor.

Fig. 11 shows the evolution of the plastic slip on the six active slip systems exemplarily for three points on the right side of the indentation axis. For the point directly next to the boundary (first row), the principal stress axis is almost aligned with the indentation axis. This stress state initially equally favors slip on systems 7, 8, 10, and 11. However, before the yield point is reached, the lattice has already rotated slightly in negative sense around the [1 1 0] axis and continues to do so. As a result, slip on systems 10 and 11 is preferred and dominates the plastic behavior. Only at the end of loading do slip systems 3 and 6 start to become active due to the negative lattice rotations reorienting these slip systems to their preferential orientation. The second point (second row in Fig. 11) is located in an area of modest lattice rotations of not more than 10°. In the course of deformation, the point actually reverts its rotation sense and finally again reaches almost its initial orientation. The principal stress axis at this point is close to a 45° angle, which favors the activation of 3/6 and
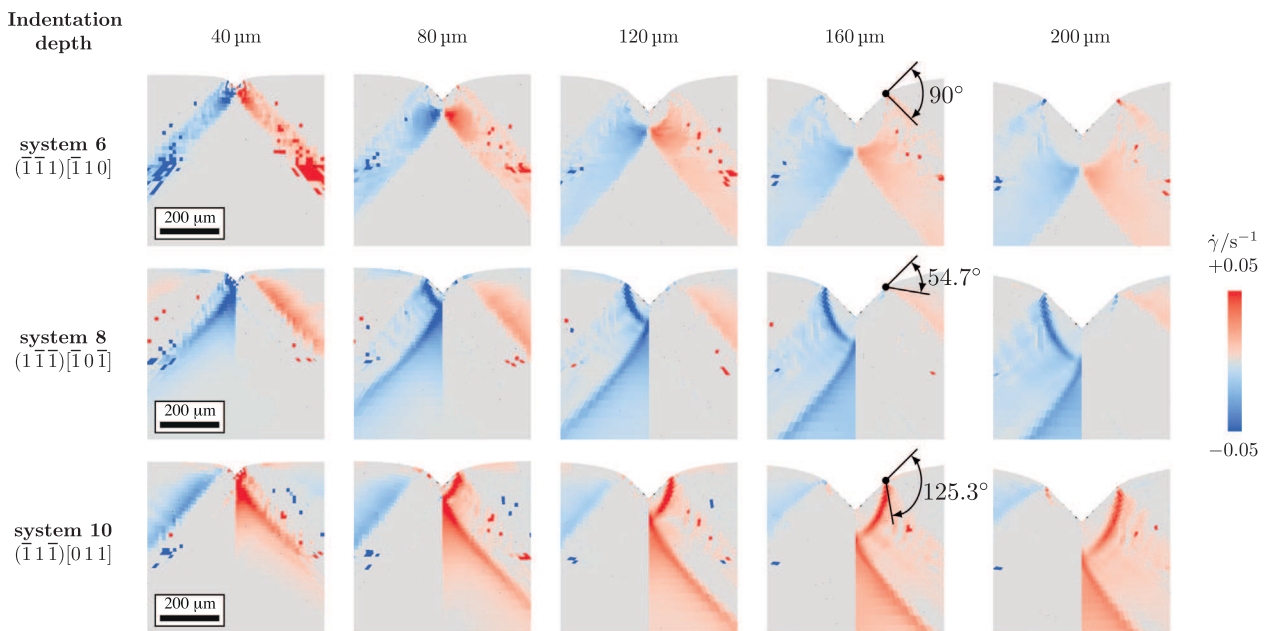


Fig. 10. Simulated plastic shear rate on slip systems ($\bar{1}$ $\bar{1}$ 1)[$\bar{1}$ 1 0], (1 $\bar{1}$ $\bar{1}$)[$\bar{1}$ 0 $\bar{1}$], and ($\bar{1}$ 1 $\bar{1}$)[0 1 1] for the wedge indent at indentation depths of 40, 80, 120, 160, and 200 μm. Contact singularity at the indenter flank is marked by black dots in the 160 μm maps. The corresponding angles indicate the analytically predicted direction of plasticity rays emanating from the contact point [58].
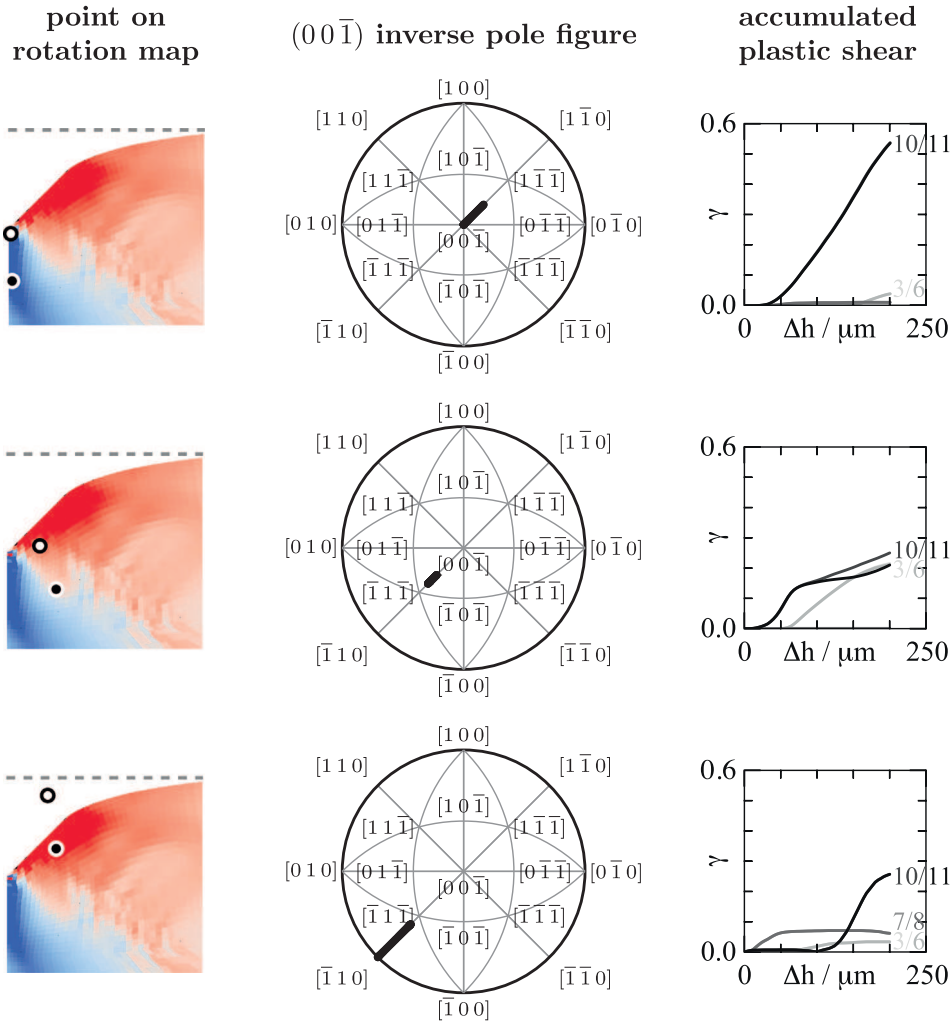
Fig. 11. Inverse pole figures and evolution of plastic shear with indentation depth $\Delta h$ for three different material points close to the wedge indent. Positions of the material points are marked in blowups of Fig. 12 in the first column (open circles correspond to position before loading, filled circles to positions at end of loading; the initial geometry is indicated by a dashed gray line). The $(0\,0\,\bar{1})$ inverse pole figures in the second column show the rotation of the principal axis of compressive stress for the respective material points (i.e. in the direction of $(y, z) = (0, -1)$ for the first point, $(y, z) = (1, -1)$ for the second point, and $(y, z) = (1, 0)$ for the third point). The third column shows evolution plots of the accumulated plastic slip on the six active slip systems 3, 6, 7, 8, 10, and 11, which always act pairwise.
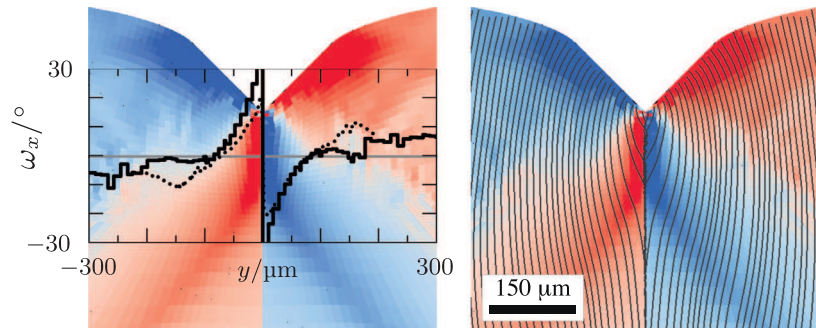


Fig. 12. Simulated in-plane lattice rotation around the wedge indent. Left: Overlay of a line plot showing the rotation across the central antisymmetry boundary along the gray line. The dotted line represents experimental values at approximately the same position reproduced from Fig. 4 in [50]. Right: Overlay of the $(0\,1\,0)$ lattice plane traces. The nominal spacing of the traces is 10 μm.

particularly 10/11, but not 7/8. The reason for slip systems 3 and 6 being activated at a later stage compared to 10/11 can be attributed to the mutual strong collinear interaction,

which requires higher stresses for activation. The last point (third row in Fig. 11) lies close to the surface. The stress axis at this point is nearly aligned with the $y$ axis. Slip

systems 7 and 8 become active first, but get less favorable for slip due to the positive lattice rotation around [1 1 0]. Plastic deformation becomes harder and enforces further lattice rotation in order to accommodate the geometrical constraints of the indenter, finally leading to such high rotations that slip systems 10/11 become favorable for slip and take over as the prevalent carriers of deformation.

### 5.3. Rotation

As seen in Fig. 5, the lattice rotation changes abruptly within a few μm across a vertical line below the indenter. More specifically, in the simulation this jump in lattice rotation occurs among neighboring integration points. If there was a gradual change in the rotation, then the lateral mesh resolution of about 5 μm does not suffice to resolve this gradient. Kysar et al. [39] specify the resolution of their orientation measurements as 3 μm, which is comparable to our simulation.

Fig. 12 shows the lattice rotation jump on a line across the vertical boundary for both simulation and experiment (experimental data reproduced from [50] at approximately the same position). The lattice rotation jump is more pronounced in the simulation than in the experiment, but the main characteristics of the rotation fields match, e.g. the distance from the boundary at which the rotation changes its sign. With increasing indentation depth, the discontinuity in the lattice rotation evolves since the left and right half of the crystal rotate away from each other. Fig. 13 illustrates the simulated evolution of the lattice rotations directly right and left of the boundary as a function of the position under the indenter. The lattice rotations quickly converge towards a maximum value of approximately $\pm 35°$ at about 30 μm below the indenter tip even for small indentation depths $\Delta h$. These high rotation differences grow further down into the material, such that at the final indentation depth of $\Delta h = 200$ μm a boundary length of more than 100 μm reveals a misorientation of 70°. The reason for this large misorientation can be understood when looking at the traces of the (0 1 0) lattice planes

around the indent shown on the right-hand side of Fig. 12. Although these lattice traces do not correspond to any slip traces in the material, they reflect the curvature of the lattice in general. As seen in Fig. 7, the specific crystal orientation does not allow for large plastic deformation at the upper indenter flanks, so that the material mainly performs a rigid-body rotation following the inclination angle of the indenter. (The orientation dependence of the rotation pattern was previously reported by Bouvier and Needleman [60].) Thus, the (0 1 0) plane traces in Fig. 12 exit the surface at an almost 90° angle. This induces counter-rotations further below in order to compensate for the unrotated lattice in the undeformed regions far below the indenter. The deeper the indenter penetrates into the material the deeper these counter-rotations extend. The same qualitative features of the (0 1 0) plane traces have also been reported by Kysar et al. [39]. However, due to the missing data close to the original indented surface, it is not possible to evaluate the angle that the trace lines draw with the surfaces. The strongly diverging traces under the indentation axis are, however, clearly visible also in the experimental data. As already pointed out by Kysar et al. [39], this indicates that a significant amount of material is transported there. Clearly, this is the material that is pushed away by the indenter above. The compression of material in this region leads to the hydrostatic pressure seen in Fig. 9.

### 5.4. Influence of dislocation transport and resulting GND density

On both sides of the rotation boundary there is an accumulation of GNDs. The reason for this is that the axis of principal compressive stress changes its direction across the indentation axis, the resolved shear stress on the active slip systems changes sign and the direction of slip is reverted. Dislocations cannot travel across the indentation axis and become stored there (see third and fourth column of Fig. 7). Most of the piled-up dislocations have edge character and belong to systems 7/8 or 10/11. As also indicated by the (0 1 0) plane traces in Fig. 12, these dislocations form a disclination under the indenter.

The pileup of GNDs around the boundary is a direct consequence of the dislocation transport and naturally evolves without any additional boundary conditions. While the GND density is related to a curvature of the crystal lattice, it is not easily possible to (inversely) derive it solely from lattice rotations. Additional assumptions have to be made, e.g. minimization of line energy or line length. The latter method was used by Kysar et al. [39] to calculate a lower bound for the GND density from the measured lattice orientations, which in the present example, indeed, equates to the exact solution when not more than two effective slip systems are active (being the case for almost the entire sample). The good match between experimental and simulated results for the GND density (see Fig. 6) thus confirms the validity of the predictions from the dislocation transport model.
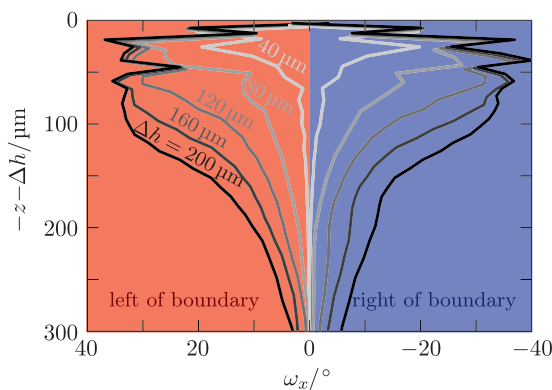


Fig. 13. Simulated lattice rotation directly left and right of the antisymmetry boundary with evolving indentation depth $\Delta h$ and along the indentation axis. The origin at $-z - \Delta h = 0$ corresponds to the indenter tip.

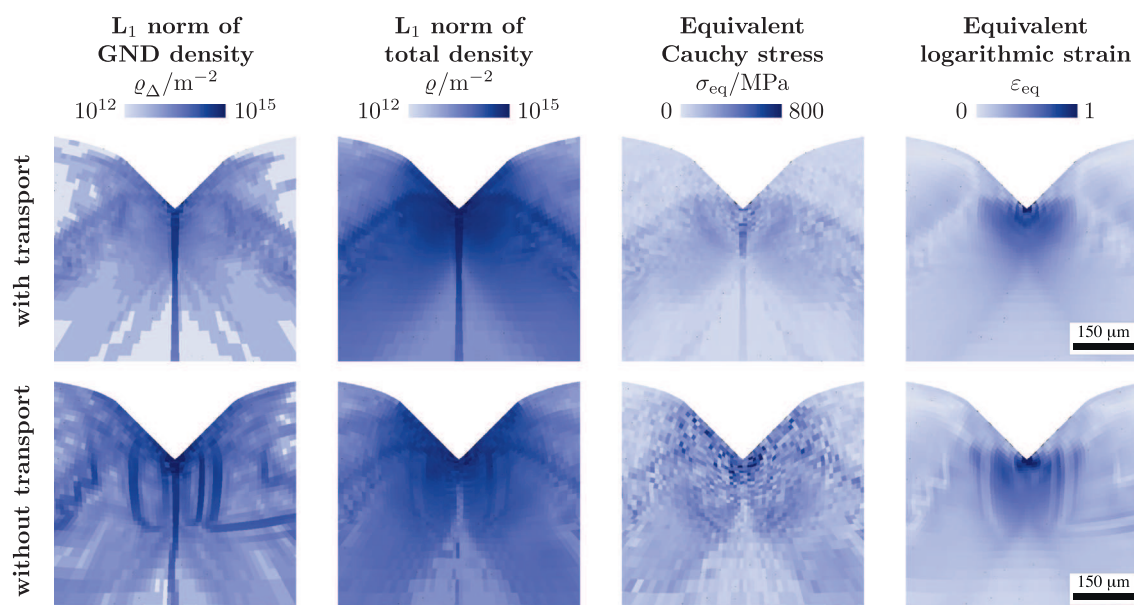| $L_1$ norm of GND density $\varrho_\Delta/\mathrm{m}^{-2}$ | $L_1$ norm of total density $\varrho/\mathrm{m}^{-2}$ | Equivalent Cauchy stress $\sigma_{\mathrm{eq}}/\mathrm{MPa}$ | Equivalent logarithmic strain $\varepsilon_{\mathrm{eq}}$ |
|---|---|---|---|
| $10^{12}$ — $10^{15}$ | $10^{12}$ — $10^{15}$ | 0 — 800 | 0 — 1 |

Fig. 14. Comparison of simulations performed with and without dislocation transport. Maps show the GND density (derived by slip gradients), the total dislocation density, the equivalent Cauchy stress after unloading and the equivalent logarithmic strain after unloading.

Since the complete deformation history of each slip system is known in the simulation, the GND density can also be derived from a gradient in the dislocation slips. We applied this method to the simulations with both the (nonlocal) dislocation transport model and a local model variant without dislocation transport. The results of the simulations are compared in Fig. 14. The maps of the GND densities in the first column reveal that the GND densities cannot adequately be reproduced from gradients in slip without dislocation transport. The local simulation overestimates the GND density with respect to the nonlocal model and even introduces features that are not visible in the experimental results. However, the importance of a correct description of dislocation transport and generation of GNDs becomes apparent in columns 2–4 of Fig. 14, especially with regard to the rotation boundary. In the absence of dislocation transport no dislocations pile up around the boundary in the local simulation (second column) and do not influence the mechanical response. In contrast, for the nonlocal model, the accumulated density at the boundary leads to an increased hardening and higher stresses that are visible as dark lines below the indenter (third column of Fig. 14). It should be emphasized that no additional gradient-dependent stress terms were used in the simulation to explicitly induce a stress field by the excess dislocations. Instead, the observed stress arises naturally from an unbalanced transport of dislocations and the resulting accumulation of density. In general, the incorporation of the dislocation transport leads to a stiffer response. In the local model, the equivalent Cauchy stress is on average lower by −20% during loading (yet slightly higher after unloading). This results in higher strains of about +10% when compared to the nonlocal model.

## 6. Conclusions

We simulated the wedge indentation of single-crystalline Ni and compared it to an experiment of Kysar et al. [39] and to more detailed data of the same experiment given by Dahlberg et al. [50]. We draw the following conclusions:

- Most of the deformation occurs in a region below the indenter of about the same size as the actual indent. However, two broad shear-bands form on both sides of the indenter that advance about five times the indentation depth into the material.
- The stress state in the material can be divided into two regions: hydrostatic pressure in a circular area around the indenter tip, and more or less uniaxial compressive stress radially pointing away from the central region. The highest stress values are found in two broad areas perpendicular to the indenter flanks.
- Only six out of the twelve fcc slip systems become activated and act pairwise in order to accomplish plane-strain deformation. In most regions of the sample, only two slip systems are active at the same time.
- A comparably low slip activity at the indenter flanks requires large rigid-body rotations in order to accommodate the geometrical constraints of the indenter. The high rotations at the indenter flank induce equally high counter-rotations below the indenter, which have different signs left and right of the indentation axis. A high gradient in the lattice rotations below the indenter arises with a maximum change from +35° to −35° within a distance of at most 5 μm. This simulated rotation pattern is in agreement with experiment, although simulated rotations are slightly too high.

- In the simulation, the rotation jump below the indenter evolves and reaches a total misorientation of about 70° after an indentation depth of 80 μm. With further indentation, the magnitude of the jump no longer changes significantly, but the lattice rotation jump propagates further down into the material.
- Due to a sign change of the resolved shear stress across the evolving boundary, dislocations pile up on both sides and form a disclination. This leads to additional hardening of the boundary in the nonlocal model due to forest hardening, which is not seen for a local model variant without dislocation transport.
- The measured lattice rotations translated into GND densities match both qualitatively and quantitatively to the simulated excess dislocation densities of the nonlocal model. GNDs can also indirectly be determined from spatial gradients in the accumulated plastic slip per each individual slip system. While this indirect method gives comparable results when applied to the nonlocal simulation results, the local model variant without transport overestimates the GND densities significantly (+215% compared to the nonlocal model, averaged over the simulated domain).
- In general, the nonlocal model behaves significantly harder during loading (stress +20%), is less compliant (strain −10%) and accumulates smaller lattice rotations (−13%, the latter values all being averages over the simulated domain).

## Acknowledgements

## References

[1] Pharr GM, Oliver WC, Brotzen FR. J Mater Res 1992;7(03):613.
[2] Oliver WC, Pharr GM. J Mater Res 1992;7(6):1564.
[3] Nix WD. Mater Sci Eng: A 1997;234–236:37.
[4] Fisher-Cripps AC. Nanoindentation. Springer; 2002.
[5] Choi Y, Van Vliet KJ, Li J, Suresh S. J Appl Phys 2003;94(9):6050.
[6] Suresh S, Giannakopoulos AE. Acta Mater 1998;46(16):5755.
[7] Gouldstone A, Koh HJ, Zeng KY, Giannakopoulos AE, Suresh S. Acta Mater 2000;48(9):2277.
[8] Sun S, Adams BL, King WE. Philos Magaz A 2000;80(1):9.
[9] El-Dasher BS, Adams BL, Rollett AD. Scripta Mater 2003;48(2):141.
[10] Wang Y, Raabe D, Klüber C, Roters F. Acta Mater 2004;52(8):2229.
[11] Field DP, Merriman CC, Allain-Bonasso N, Wagner F. Model Simul Mater Sci Eng 2012;20(2):024007.
[12] Zaafarani N, Raabe D, Singh RN, Roters F, Zaefferer S. Acta Mater 2006;54(7):1863.
[13] Zaafarani N, Raabe D, Roters F, Zaefferer S. Acta Mater 2008;56(1):31.
[14] Demir E, Raabe D, Zaafarani N, Zaefferer S. Acta Mater 2009;57:559.
[15] Kocks UF. J Eng Mater Tech (ASME-H) 1976;98:76.
[16] Mecking H, Kocks UF. Acta Metall 1981;29:1865.
[17] Roters F, Raabe D, Gottstein G. Acta Mater 2000;48(17):4181.
[18] Kröner E. Kontinuumstheorie der Versetzungen und Eigenspannungen, Ergebnisse der angewandten Mathematik, vol. 5. Berlin: Springer; 1958.
[19] Nye JF. Acta Metall 1953;1(2):153.
[20] Bilby BA, Gardner LRT, Smith E. Acta Metall 1958;6(1):29.
[21] Ashby MF. Philos Magaz 1970;21(170):399.
[22] Kröner E. Int J Eng Sci 1963;1(2):261.
[23] Trivedi PB, Yassar RS, Field DP, Alldredge R. Mater Sci Eng: A 2006;425(1–2):205.
[24] Kubin LP, Mortensen A. Scripta Mater 2003;48(2):119.
[25] Motz C, Schöberl T, Pippan R. Acta Mater 2005;53(15):4269.
[26] Nix W, Gao H. J Mech Phys Solids 1998;46(3):411.
[27] Gao H, Huang Y, Nix WD, Hutchinson JW. J Mech Phys Solids 1999;47(6):1239.
[28] Gao H, Huang Y. Scripta Mater 2003;48(2):113.
[29] Gurtin ME. J Mech Phys Solids 2002;50(1):5.
[30] Acharya A. J Mech Phys Solids 2001;49(4):761.
[31] Walgraef D, Aifantis EC. Int J Eng Sci 1985;23(12):1351.
[32] Groma I, Csikor FF, Zaiser M. Acta Mater 2003;51(5):1271.
[33] Arsenlis A, Parks DM. J Mech Phys Solids 2002;50(9):1979.
[34] Sandfeld S, Hochrainer T, Zaiser M, Gumbsch P. J Mater Res 2011;26(05):623.
[35] Sedláček R, Kratochvíl J, Werner EA. Philos Magaz 2003;83(31):3735.
[36] Hochrainer T. Evolving systems of curved dislocations: mathematical foundations of a statistical theory. Ph.D. thesis, Universität Karlsruhe (TH), Aachen; 2006.
[37] Sandfeld S, Hochrainer T, Gumbsch P, Zaiser M. Philos Magaz 2010;90(27–28):3697.
[38] Yefimov S, Groma I, van der Giessen E. J Mech Phys Solids 2004;52(2):279.
[39] Kysar JW, Saito Y, Oztop MS, Lee D, Huh WT. Int J Plast 2010;26(8):1097.
[40] Roters F, Eisenlohr P, Hantcherli L, Tjahjanto DD, Bieler TR, Raabe D. Acta Mater 2010;58:1152.
[41] Bilby BA, Gardner LRT, Stroh AN. In: Proceedings of the 9th international congress on applied mechanics, vol. 8. Bruxelles: Université de Bruxelles; 1957. p. 35–44.
[42] Rice JR. J Mech Phys Solids 1971;19:433.
[43] Ma A, Roters F. Acta Mater 2004;52(12):3603.
[44] Friedel J. Dislocations. Reading, Massachusetts: Addison-Wesley; 1964.
[45] Essmann U, Mughrabi H. Philos Magaz A 1979;40(6):731.
[46] Seeger A. Philos Magaz Ser 7 1954;45(366):771.
[47] Franciosi P, Zaoui A. Acta Metall 1982;30:1627.
[48] Kubin L, Devincre B, Hoc T. Acta Mater 2008;56(20):6040.
[49] Kocks UF, Argon AS, Ashby MF. Progr Mater Sci 1975;19:1.
[50] Dahlberg CFO, Saito Y, Öztop MS, Kysar JW. Int J Plast 2014;54:81.
[51] Hirth JP, Lothe J. Theory of dislocations. New York: John Wiley & Sons; 1982.
[52] Tippelt B, Breitschneider J, Hähner P. Phys Status Solidi A 1997;163(1):11.
[53] Gottstein G. Physikalische Grundlagen der Materialkunde. Berlin: Springer; 2007.
[54] Keller C, Hug E, Chateigner D. Mater Sci Eng A 2009;500(1–2):207.
[55] Cordero B, Gómez V, Platero-Prats AE, Revés M, Echeverría J, Cremades E, et al. Dalton Trans 2008(21):2832.
[56] Karthik V, Visweswaran P, Bhushan A, Pawaskar DN, Kasiviswanathan KV, Jayakumar T, et al. Int J Mech Sci 2012;54(1):74.
[57] Rice JR. Mech Mater 1987;6:317.
[58] Saito Y, Kysar JW. Int J Plast 2011;27(10):1640.
[59] Saito Y, Oztop MS, Kysar JW. Int J Plast 2012;28(1):70.
[60] Bouvier S, Needleman A. Model Simul Mater Sci Eng 2006;14(7):1105.